Experimental study of the planar-to-cellular transition during thin-film directional solidification: Observations of the long-time-scale dynamics of microstructure formation

J. T. C. Lee* and R. A. Brown
Department of Chemical Engineering, Massachusetts Institute of Technology, Cambridge, Massachusetts 02139
(Received 26 March 1992)

The morphological evolution of the crystal-melt interface formed during the thin-film directional solidification of the succinonitrile-acetone alloy is studied using an experimental system that permits extremely-long-time-scale experiments under conditions close to those for the onset of cellular growth from the planar interface. Long exposure times of the alloy to high temperatures result in thermal decomposition of the succinonitrile, which increases the total concentration of solute or impurity in the sample. This effect alone may be responsible for the apparent hysteresis observed by others in the measurement of the critical solidification rate V_c for the onset of cellular growth and may explain the differences between those experiments and numerical calculations. We show that the evolution of the planar interface into cellular structures occurs first in packets of more rapidly growing undulations separated by regions of slower growing cells. These cellular structures propagate over the entire interface and at very long times the interface exhibits shallow cells without a selected wavelength. The interface dynamics appears to be spatiotemporally chaotic. The wavelength distribution is dispersed about a mean that is almost a factor of 4 below the critical value expected from linear stability theory. Deeper cells exhibit stronger wavelength selection behavior and are observed at solidification rates only slightly above V_c; the mean wavelength increases with increasing V for deep cells.

I. INTRODUCTION

The transition during solidification of a binary alloy in an unidirectional temperature field from a planar interface to one with fine-scale microstructure is one of a growing collection of pattern-forming phenomena in physicochemical systems. As in other examples, the planar interface becomes unstable at a critical value of the control parameter, either growth rate or temperature gradient, which should be predictable from linear stability theory applied to an accurate model for microscale crystal growth. For a two-dimensional solidification system, theory predicts that the initially nonplanar state has small-amplitude sinusoidal cells which grow as the control parameter is increased. Deep cells and finally dendrites are observed experimentally with increasing growth rate. The values of growth rate, temperature gradient, and alloy concentration for these transitions and the shapes and length scales associated with the cells and dendrites depend on the phase diagram of the alloy, on the surface free energy between the melt and crystal, and on the transport of heat and solute in both phases. Over the last 25 years, a large amount of theoretical, computational, and experimental research has aimed at predicting and measuring these transitions and at determining the evolution of the length scales associated with the interface, the cellular wavelength, and later the interdendritic spacing and side branching of the dendrites. An important issue is whether these length scales are selected uniquely by the choice of operating conditions or are picked only as the mean of a band of values. This issue is manifest in the question of wavelength selection for cellular growth that is addressed in these experiments.

The simple thermodynamic argument of Tiller and Rutter[1] predicts the relationship between the control parameters for the onset of the instability as

$$V > \frac{DGk}{mc_0(1-k)} , \tag{1}$$

where G is the temperature gradient, c_0 is the alloy concentration, V is the growth rate, k is the equilibrium partition coefficient, m is the slope of the liquidus curve, and D is the diffusion coefficient of the solute in the melt. As discussed by Coriell, McFadden, and Sekerka,[2] this simple result predicts the relationship between the control parameters near onset in many systems, but gives no information about the length scales associated with the microstructure. Supplying this information requires detailed models that include the evolution of heat and solute transport along the interface and that account for the interfacial properties of the melt-crystal interface. One of the goals of experiments has been to support the development of such theories. Clearly, the ability of models to predict microstructure formation must begin with the initial transition from a planar to a cellular interface structure. One goal of the experiments reported here is to study carefully the dynamics of cellular interface formation at conditions very close to the onset of microstructure formation from a planar interface.

Mullins and Sekerka[3] predicted the conditions for the instability of a planar interface during the two-dimensional solidification of a binary alloy. The most important result of this linear analysis is a neutral stability curve that predicts the dependence of the critical value for the control parameter on the spatial wavelength (λ) or wave number ($\nu=\lambda^{-1}$) of the small-amplitude cellular

structure; henceforth, we will use the growth rate V as the control parameter and consider experiments in which V is varied and G and c_0 are fixed. The most dangerous wavelength λ_c—and the one expected to be observed in an experiment—corresponds to the minimum value of V, i.e., $V_c = V(\lambda_c)$. The primary goal of experiments aimed at detecting the onset of cellular solidification is to measure V_c and λ_c as a function of temperature gradient and alloy concentration. Theoretically, the onset of cellular forms corresponds to a bifurcation from the planar state to steadily solidifying cellular morphologies with spatial wavelength λ_c that evolve with changing growth rate V. This perspective is crucial to understanding the evolution of thin-film solidification experiments and is reviewed below.

Jackson and Hunt[4] used transparent organic alloys and thin-film solidification experiments as a prototype for two-dimensional directional solidification experiments. Here a thin sample of an organic alloy that solidifies into a plastic crystal is placed in the thin gap between two small glass plates—nominally microscope slides—and is moved through a temperature gradient established between a heater and cooler. The microstructure of the interface is observed with an optical microscope. Since this work, a host of experimentalists have studied thin-film solidification; see Refs. 5–12 and the review in Ref. 13. Most notable are the experiments of three groups: the experiments of de Cheveigné and co-workers[5,7] are based on an alloy of carbon tetrabromide and an impurity thought to be bromine formed by photo- (and possibility thermal) decomposition; Eshelman, Seethavaman, and Trivedi use succinonitrile-acetone (SCN-ACE) alloys;[9,10] and the work of Libchaber and co-workers is based on the isotropic-to-nematic phase transition in a liquid-crystal material caused by a directional temperature gradient imposed along a thin sample.[6,11,12]

These studies have documented a myriad of nonlinear dynamical phenomena in cellular solidification that evolve after the onset of cellular growth. Phenomena include the development of deep solidification cells for growth rates just above V_c, splitting of individual cell tips as a mechanism for decreasing the spatial wavelength,[5] traveling waves that result in lateral migration of the cellular pattern along the interface,[6,7] and the onset of dendritic growth.[7,10] These observations are important to the question of the uniqueness of the cellular wavelength discussed below.

Although the onset of cellular growth is unmistakable in these experiments, the direct comparison with the results of linear stability theory has proven very difficult. For organic solidification systems that are reasonably well characterized, such as the succinonitrile system of Eshelman and Trivedi,[9] the spatial wavelength observed near onset is significantly smaller than that predicted by linear stability theory. Moreover, the smallest-amplitude cells that are observed do not look like the sinusoidal forms expected for the disturbance to the interface, but have more blunt tips separated by deep and slender grooves. Similar results are reported for the bromine-carbon tetrabromide systems.[5] In fact, the best example of the linear instability to date is the study of the isotropic-to-nematic phase transition in a liquid-crystal system,[11] where sinusoidal cells are seen, as is the linear relationship between V_c and G^{-1} predicted by Eq. (1).

Several explanations for the difficulty in observing linear instability have been suggested, based on the experiments and on theory and computations. These include the possibility for subcritical bifurcation from the planar state, which leads to hysteresis in the observation of finite-amplitude cells; imperfections in the thin-film system caused by the three dimensionality of the sample, which significantly alter the nonlinear transition to cells; and the occurrence of nonlinear transitions to cells with other wavelengths and to time-dependent dynamical states which are superimposed on the initial linear instability. One of the major objectives of our experiments has been to differentiate between these possibilities.

To understand these arguments requires background from the analysis of solidification models. We concentrate on the predictions of the so-called solutal model,[14] in which the temperature gradient across the sample is assumed to be set, irrespective of the shape of the melt-solid interface and the evolution of the microstructure is determined by the redistribution of a dilute solute and by its interaction with the interface through the liquidus temperature and the interface curvature. We have investigated the solutal model for two-dimensional directional solidification using weakly nonlinear analysis and numerical simulation.[14–20] The predictions of these calculations are summarized qualitatively for the succinonitrile-acetone system used in our experiments.

(i) The neutral stability curve $V_c = V(\lambda_c)$ for the alloy concentrations of interest are extremely flat; for V only slightly greater than V_c, a band of wavelengths is unstable. This flatness is demonstrated in Fig. 1 by the neutral stability curve for a succinonitrile-acetone alloy with $c_0 = 0.1$ mol % acetone and $G = 60$ K/cm. Here a 2% increase in V above V_c leads to instability in a band of

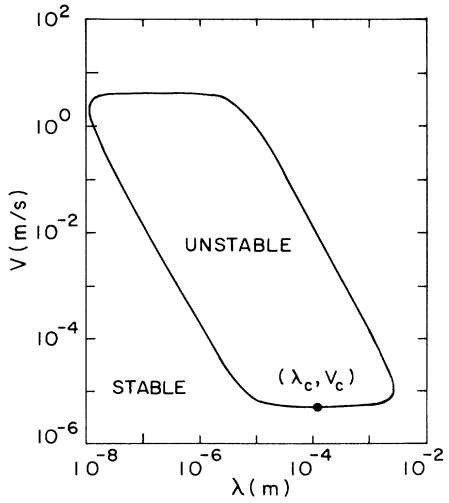

FIG. 1. Neutral stability curve for the SCN-AC alloy with $c_0 = 0.1$ mol % acetone and $G = 60$ K/cm.

wavelengths that stretches approximately from $\lambda_c/4$ to $10\lambda_c$.

(ii) The initial evolution of the cellular forms with wavelength λ_c may be either subcritical or supercritical with respect to changing V from V_c. However, the range of the subcriticality predicted from two-dimensional models is extremely small, when it exists.[14,18] For the alloy system shown in Fig. 1, the evolutions of cells with wavelength λ_c is subcritical, i.e., to lower values of V only for growth rates down to $V=V_{c-}=0.975V_c$, at which point the evolution changes direction and evolves to higher values of growth rate. Because the subcritical portion of the branch is temporally unstable, hysteresis is expected in the observation of cellular forms in the range $V_{c-}<V<V_c$; however, this gap (V_c-V_{c-}) may be too small to be observable.

(iii) The flatness of the neutral stability curve also leads to nonlinear interactions of families of cell shapes with spatially resonant wavelengths. These interactions take the form of secondary bifurcations between families of solutions and lead to decreasing wavelength by a mechanism that looks like tip splitting. This evolution to smaller wavelengths through secondary bifurcations has been predicted by asymptotic analysis,[20,21] computations,[14,17,18] and observed in experiments.[5] For the SCN-ACE system shown in Fig. 1, cells with wavelength λ_c only exist for $V<1.01V_c$; hence, only cellular wavelengths smaller than λ_c are expected to be observed.

(iv) The flatness of the curve also leads to other nonlinear interactions, such as parity-breaking transitions that lead to traveling waves in the cellular forms.[19,21,22] These traveling waves have been observed in experiments.[7,8]

(v) Computations with collections of cells predict complicated dynamics involving cell birth by the tip-splitting mechanism, cell death by dissolution in the grooves between cells, and cell migration along the interface.[17,19] These dynamics occur on very long time scales—corresponding to thousands of diffusion times defined on the length scale of a single cell—and may be chaotic. Moreover, the time scale for the growth of linear instability for growth rates near onset may be extremely small. For example, the exponential growth rate computed from linear stability theory is only 1×10^{-4} s for $V=1.1V_c$ and the most dangerous spatial wavelength. This result implies that finite-amplitude cells are expected to develop over hundreds to thousands of seconds and long-time-scale experiments are needed to observe this transition. Moreover, the interface does not exhibit a single wavelength for given (V,G,c_0).

Each of the potential mechanisms for the difficulty associated with the observation of the linear stability is discussed in turn. The most often cited reason for the problem is the initial subcritical evolution of the cellular forms; because the small-amplitude cellular states exist at lower values of V, they are expected to be unstable and unobservable. Moreover, the stable finite-amplitude states cells are expected to exhibit hysteresis, as depicted in Fig. 2. The observed onset will be near V_c, but finite-amplitude cells are expected to exist for $V_{c-}<V<V_c$. Hysteresis was observed by Herslot and Libchaber[23] and later by others.[9,24,25] De Cheveigné, Guthmann, and Lebrun[5,24] reported values of V_{c-} that were 25% lower than the value for the observed onset of the cells in the CBr_4-Br_2 system and attributed this hysteresis to the subcritical bifurcation. This result does not agree with calculations by Ramprasad[25] for the thermophysical properties of this system and the two-dimensional solutal model, which indicate that the range of the subcriticality under the conditions of the experiment should be less than 0.1% of V_c.

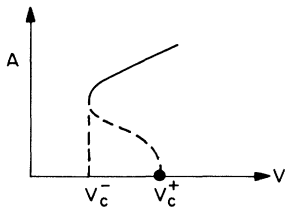

FIG. 2. Schematic of hysteresis in the critical value of growth rate for the onset of cellular growth expected with subcritical evolution of the cellular forms.

We believe that continuing thermal decomposition of the CBr_4 is responsible for this discrepancy. Our argument is based on the data for the thermal decomposition of CBr_4 of Frederick and Hildebrand,[26] who report thermal decomposition for pure CBr_4 to be 0.04 mol % when the material is exposed to a temperature of 102 °C for 5 h. We estimate that a typical sample in the experiments reported in Ref. 5 was exposed to temperatures of at least this magnitude for over 3 h. If a decomposition of 0.04 mol % does occur, this amount of impurity is equal to approximately one-third the level of Br_2 estimated by the researchers to be present in the sample. Applying the constitutional supercooling criterion [Eq. (1)] to this larger composition predicts a reduction in the onset growth rate by 30%. This reduction is consistent with the measurements of hysteresis reported in both Refs. 5 and 24.

Eshelman and Trivedi[9] have reported hysteresis in the onset growth rate for experiments with 0.1 wt. % acetone in succinonitrile. Again, the range of growth rates in the hysteresis is much larger than predicted by simulation. Interestingly, Eshelman and Trivedi[9] observed the development of very deep cells in only a few minutes. Although the details of each experimental run are not reported, we have estimated the exposure time for each experiment as 15 h; reuse of a particular sample will increase the total exposure time. We demonstrate in Sec. III C that measurable decomposition of SCN occurs for exposure times in excess of 30 h.

Differences between the thin-film experiment and the two-dimensional models that form the basis for the predictions may explain the differences between predictions and observations. The three dimensionality of the thin-film solidification system leads to imperfections in the system that significantly alter the onset and form of the transition. Ungar and Brown[27] demonstrated that grain boundaries along a two-dimensional, almost planar inter-

face serve as imperfections and move the onset point for subcritical behavior to lower values of V. Caroli, Caroli, and Roulet[28] used weakly nonlinear analysis to reach the same conclusion for the imperfection caused by the curvature of the interface across the gap of the sample. Unfortunately, there are no indications for the range of validity of the asymptotic predictions in Ref. 28; comparisons between weakly nonlinear analysis and numerical simulations of directional solidification in other contexts have demonstrated very limited range of validity[14,20] for organic solidification systems.

We believe that the difficulty in observing the transition to small-amplitude cells is connected with the flatness of the neutral stability curve and with the tendency for solidification systems to undergo secondary nonlinear transitions at growth rates just slightly above V_c, so that the onset of the small-amplitude cells predicted by linear theory is only observable for a vanishingly small range of growth rates. Moreover, these dynamical interactions lead to a decrease in the spatial wavelength from λ_c for very small increases in V; this prediction agrees with the existing experimental data for alloy solidification, where the wavelengths observed near onset are substantially below the value of λ_c predicted for the parameters of the experiment.[5,9]

The observations of Oswald, Bechhoefer, and Libchaber[11] of small-amplitude cells for the liquid-crystal system are the single experimental result that clearly appears to be in the regime of linear theory. This is expected from a comparison of what is known about the thermophysical properties of this system and the organic directional solidification experiments. Although modeling of the liquid-crystal system is relatively imprecise, the analogy with the directional solidification system indicates a much more dominant role of the surface free energy in the linear stability analysis, which results in much greater curvature of the neutral stability curve; see the discussion in Ref. 12. As a result, the nonlinear interactions, such as the secondary bifurcations that lead to tip splitting, are pushed to higher relative growth rates[29] and do not mask the linear instability.

Our experimental study is focused on the long-time-scale dynamics of pattern formation in the planar-to-cellular transition at growth conditions very close to the critical growth rate V_c predicted by linear theory. We demonstrate that linear stability theory is not observed within the accuracy of this experiment and that complex, time-dependent patterns develop at long times for growth conditions very close to the critical growth rate.

These results also have important implications for theories of wavelength selection during cellular growth, a recent topic of much theoretical and computational effort.[16,19,30] It is understood that there is no mechanism for selecting a unique wavelength for $V > V_c$ based solely on the existence of steadily solidifying two-dimensional cells.[16,31] Ramprasad, Bennett, and Brown[16] computed steadily solidifying cells for a range of wavelengths for given growth conditions; no unique wavelength exists. Moreover, the transient simulations in Refs. 17 and 19 indicate that the interface continually evolves dynamically through the splitting of cell tips, lateral migration of cells, and cell dissolution in the grooves between the cells. Then the cellular wavelength must be defined as a spatially and temporally averaged quantity. The experiments shown here bear out this picture for shallow cells.

The experimental apparatus is designed especially for this purpose and is described in Sec. II. The calibration of the experiment is described in Sec. III and documents the importance of thermal decomposition on the interpretation of the results. Analysis of several experiments is presented in Sec. IV and shows the development of patterns with spatiotemporal chaos.

II. EXPERIMENTAL METHODS

The transparent organic alloy composed of succinonitrile (1,2-dicyanoethane, $NC(CH_2)_2CN$) doped with dilute concentrations of acetone (0.1–0.5 mol %) is the system of choice for observation of microstructure in directional solidification experiments. Succinonitrile is in the class of transparent, organic crystals first suggested for this purpose by Jackson and Hunt,[4] because these materials solidify without facets and thus emulate metallic systems. The succinonitrile-acetone (SCN-ACE) system is uniquely suitable for fundamental experimental studies because its thermophysical properties are known precisely (Table I) from the extensive measurements by Chopra, Glicksman, and Singh[36] and because high-purity material (99.9995 mol %) is available.[37]

The thin-film directional solidification system used in the experiments reported here is designed specifically for careful control of conditions near the onset of cellular solidification. A schematic of the apparatus is shown as Fig. 3. The sample cell is extremely long, so that long-time-scale dynamics can be observed. Both the growth rate and temperature gradient are controlled to be constant over the length of an experiment. Ranges for these parameters were determined from linear stability analysis using characteristic values for the acetone concentration c_0 and the temperature gradient G; a sample linear stability curve for $c_0 = 0.2$ mol % and $G = 60$ K/cm is shown in Fig. 1. For typical operating conditions, the range of critical growth rates for the onset of cellular forms is predicted to be $0.5 \leq V_c \leq 2.5$ μm/s and the most dangerous wavelength is $100 \leq \lambda_c \leq 1000$ μm. We have designed the apparatus to be sufficiently wide to accommodate 100–1000 cells and long enough for experiments of up to 10 000 diffusion time units t_d defined as λ_c^2/D.

Thin-film experiments, such as the one described here, are not a perfect representation of a two-dimensional solidification system, because of the present of the third thin dimension for the sample. Because it is impossible to make the temperature constant in this direction, the melt-crystal interface is necessarily curved in the narrow dimension. Also, preferential wetting of the glass plates by the melt may introduce curvature in the interface as well. An analysis by Caroli, Caroli, and Roulet[28] has demonstrated that surface curvature supplies an imperfection to the classical linear stability analysis and leads to singular behavior near the onset of cellular growth. This behavior is most pronounced where the initial bifurcation is subcritical, i.e., to lower values of the growth

TABLE I. Thermophysical properties of succinonitrile and the succinonitrile-acetone alloy.

Properties of succinonitrile	Value	Comments
Molecular weight (M_{SCN})	80.092 g/mol	
Density of solid (ρ_s)	1.016 g/cm^3	extrapolated to melting point
Density of melt (ρ_m)	0.988 g/cm^3	at melting point
Equilibrium melting point (T_0)	58.09°C	
Heat of fusion (L)	3702.8 J/mol	
Specific heat of solid (C_{ps})	153.21 J/mol K	at melting point
Specific heat of melt (C_{pl})	160.18 J/mol K	at melting point
Thermal conductivity of solid (k_s)	2.24×10^{-3} J/cm s K	at melting point
Thermal conductivity of melt (k_l)	2.23×10^{-3} J/cm s K	at melting point
Melt-t-solid interfacial energy (γ_{sl})	8.95×10^{-7} J/cm^2	at melting point
Properties of succinonitrile/acetone alloy	**Value**	**Comments**
Diffusion coefficient (D)	1.27×10^{-5} cm^2/s	
Slope of liquidus curve (m)	−2.22 °C/mol % acetone	
Partition coefficient (k)	0.1	

rate; in this case, a singular transition occurs in the solution structure and the abrupt transition between a stable planar and cellular interface is predicted to widen, with the onset moving to lower values of V.

Several experiments have reported measuring the dependence of the critical velocity on the gap thickness in the thin direction.[5,10] They found a lower bound below which V_c is dependent on the thickness. We have not attempted to factor out the dependence on spacing in the experiments reported here. We use a gap spacing that is just below the lower bound reported by Eshelman, Seetharaman, and Triverdi[10] for a similar SCN-ACE alloy.

A. Experimental system

1. Heat-transfer system

The sample cell is constructed from $\frac{1}{4}$-in.-thick glass plates that measure 1000 mm long by 76 mm wide. The thin solidification sample is constructed by separating these plates by a 75-μm-thick Teflon gasket. The glass plates are sealed on all four sides using silicon rubber while the glass is pressed against the gasket. The SCN-ACE alloy is added through fill holes located at each end of the top glass plate. The effective sample dimensions are 945 mm long by 45 mm wide after accounting for the area occupied by the gasket and sealant. The sample cell is translated by a long travel translational table through a temperature gradient that is established by heating and cooling units set at temperatures such that the interface lies between them.

The heating unit is powered by ten cartridge heaters (Fenwal Inc.) embedded in a machined copper block; eight heaters are rated for a maximum power output of 580 J/s and the other two for 550 J/s. The temperature is maintained by a P.I.D. controller (Omega model CN2000). The temperature of the heating block is input to the temperature controller and is measured by a resistance temperature detector (RTD) that is bonded to the inner surface of the heating block. The cooling unit consists of a copper cooling block which surrounds the sample holder. The block is cooled by passing a commercial refrigerant (R502) through cooling coils that are sandwiched into the cooling block. The block is connected to a refrigeration system (Low-Temp Engineering Inc.) with a 5560-J/s capacity.

The performance of the heat-transfer system was estimated, and the heater and cooler were designed from model calculations based on a quasi-one-dimensional heat-transfer analysis: See Lee[32] for details. Several features of this model are worth mentioning. First, the analysis is based on modeling conduction across the thickness of the sample using an effective thermal conductivity for the glass plates and the sample and making the fin approximation.[33] The change of the thermal conductivity and latent heat release upon phase change are ignored. Both of these are good approximations for the SCN-ACE system solidifying at very slow rates. The

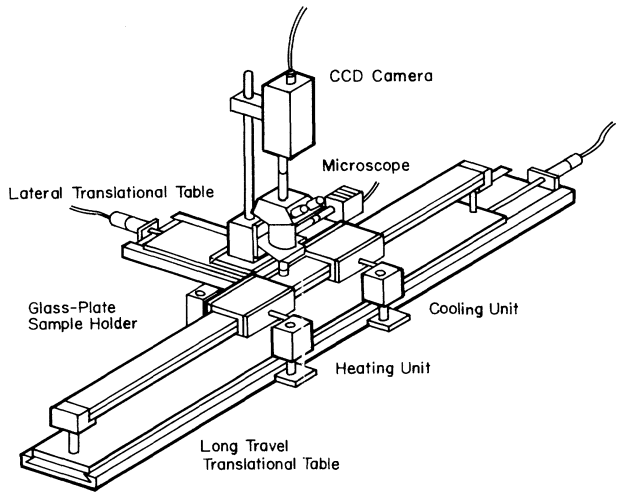

FIG. 3. Schematic of large-scale apparatus for thin-film solidification.

cooler and heater were modeled as constant-temperature energy sources with heat transfer to the sample by conduction, convection, and radiation accounted for by heat-transfer coefficients.

The one-dimensional model formally should be valid when heat transfer from the surface of the sample to either the ambient, heater, or cooler is small compared to the heat flux in the axial direction. This scaling is represented by the Biot number defined as $N_{Bi} = hb/k_s$, where h is the heat-transfer coefficient from the surface of the sample, b is the half thickness of the sample holder, and k_s is the effective thermal conductivity of the sample. The value of N_{Bi} varies because of the different heat-transfer environments supplied by the heater, cooler, and ambient, but is everywhere in the range $0.05 \leq N_{Bi} \leq 0.3$.

An important result of the modeling is shown in Fig. 4 for a 5-cm separation between the heater and cooler; the temperatures measured on the heater and cooler were 199.8 and $-26.3\,^{\circ}C$, respectively, and were used as input into the model. The temperature gradient is not constant along the axis of the sample in either the model analysis or the experimental measurements. The predictions of the model for the axial temperature profile were compared directly to measurements of the surface temperature of the glass plate. Surface temperature measurements were made using a surface probe composed of a small, spring-loaded Chromel-Alumel temperature-sensing element (Omega 88008) and are shown by the circles in Fig. 4. The variation of the axial temperature gradient is apparent in the measurements as well. The variation increases toward the hot zone; between points A and B in Fig. 4 the gradient is estimated as $-20\,^{\circ}C/cm$, while it is approximately $-14\,^{\circ}C/cm$ between points B and C.

The temperature of the surface is overpredicted by the model near the heater. This is probably an indication that the one-dimensional approximation is not accurate in this region and that a temperature gradient exists across the thickness of the sample holder near the heater. The existence of this vertical temperature gradient is consistent with the abrupt change in heat transfer between the ambient and heater as the sample goes into the heater. Elementary heat-transfer analysis leads to the conclusion that the temperature field should be two-dimensional for a distance closer than $O(1\text{ cm})$ from the heater. This prediction is consistent with the measurements in Fig. 4.

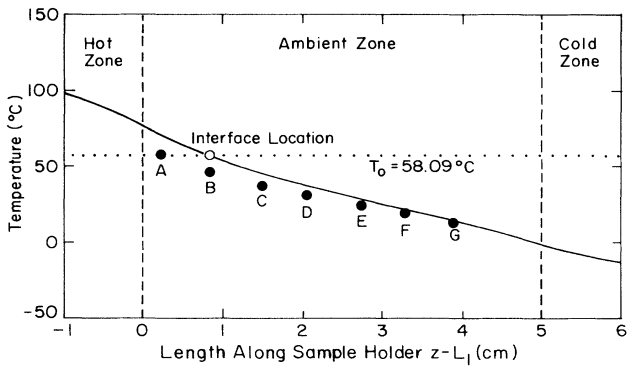

FIG. 4. Comparison of axial temperature profiles predicted from the quasi-one dimensional heat-transfer model and measured on the surface of the sample.

Because of the temperature variations observed near the heater, experiments reported here were performed with the metal-crystal interface biased slightly toward the cooler, where the model and measurements are in good agreement. The temperature gradients reported throughout this study are those measured with the surface probe.

2. *Translation system*

A microtranslation system driven by a direct current motor (Micro Kinetics Corp.) propels a long translation table by a precision rolled ball screw. The precision of the drive rate was controlled by a gear-motor assembly with an exceptionally large gear ratio: Translation rates in the range 0.5–2.3 μm/s were produced with a gear ratio of 98 070:1. The translation rate is set by a speed controlled for the motor and has an accuracy of ± 0.02 μm/s, as established by an independent optical scale. Translation rates of 0.40–8.3 μm/s are achievable by changing the motor speed and gear ratio.

3. *Imaging system*

The microstructure of the melt-solid interface was recorded using a CCD camera with 610×485 pixel resolution (each measuring 9.9 μm $\times$ 18.6 μm) attached to a bright-field-illumination metallurgical microscope (Olympus, model BHMJ). The microscope is used with $5\times$ magnification. Using this objective, each pixel represents an area of 1.5 μm^2, which is almost two orders of magnitude below the characteristic cellular wavelength for linear instability.

As shown in Fig. 3, the microscope and camera are translated laterally along the interface using a Micro Kinetics translation mechanism. Interfacial widths of 6340–12 680 μm are recorded on video tape and the images are digitized to yield the interface shapes. Spectral decomposition of the digitized images is performed using the fast-Fourier-transform (FFT) algorithm.[34] The processing is performed by a RTI (Recognition Technologies Inc.) pixel-processing station; for details, see Lee.[32] Long samples of the interface are imaged by translating the camera and connecting the images for these sections; an image of a flat interface constructed this way is shown with its FFT as in Fig. 5. Note that the splicing of the interface that occurs at separations of 600 μm results in a peak in the power spectrum with intensity of only 0.5. As described below, the magnitude of this peak is small compared to other features in the spectrum. Also note that no large-angle grain boundaries are apparent along the interface.

4. *Succinonitrile-acetone samples*

Succinonitrile has been well characterized[35,36] for use in prototypical solidification experiments. Samples used here are ultrapure [99.9995; melting temperature

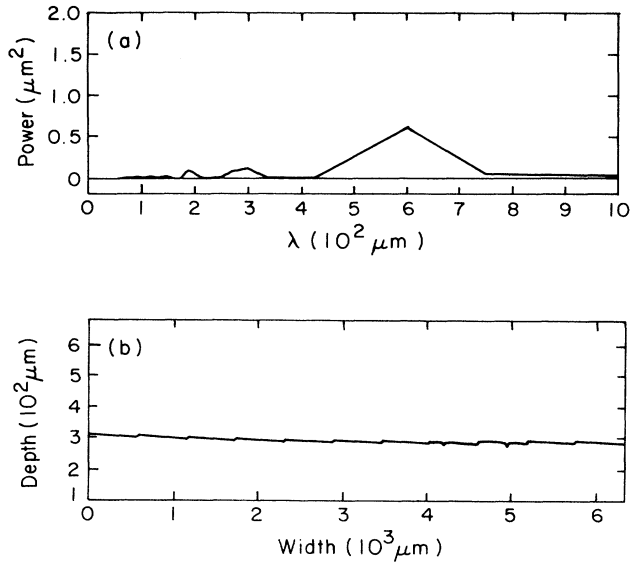

FIG. 5. Power spectra and digitized interface shape taken for a planar interface.

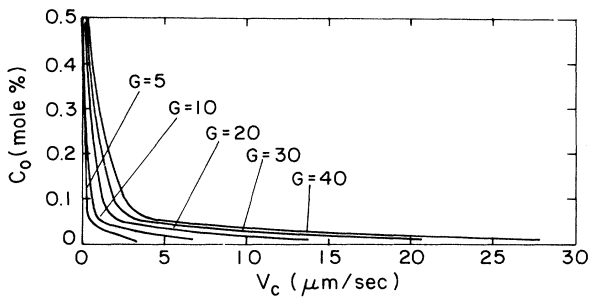

FIG. 6. Dependence of the critical growth rate V_c predicted by linear stability theory on the concentration c_0 and temperature gradient G for SCN-ACE alloy.

331.24±0.03 K (Ref. 37)] as obtained from Glicksman at Rensselaer Polytechnic Institute. Two sample-preparation procedures were tested for addition of the acetone to the succinonitrile; the first was performed under partial vacuum, and the second was done using a nitrogen atmosphere. In both methods, the succinonitrile is moved from a hermetically sealed container to a glass apparatus where it is melted and the acetone is added using a microsyringe. The mixed alloy is moved to the sample holder by attaching the glass cylinder via a ground glass joint to the heated sample holder, melting the sample and allowing it to fill under gravity. The sample is allowed to solidify after filling.

In the first method, the mixing and filling procedures are carried out under partial vacuum; in the second, it is done under a nitrogen atmosphere. Different final acetone concentrations seem to result from these methods because of acetone loss during mixing of the alloy and filling of the sample cell. As expected, more acetone is lost during the mixing and filling stages when the vacuum is used than when the procedure is done under a nitrogen atmosphere.

In any case, precise control of the added acetone is not possible with this system. The acetone concentration is estimated by using the constitutional supercooling (CS) criterion [Eq. (1)] with the measured values substituted for growth rate and temperature gradient. This limitation prevents comparison between the experiments and the predictions of linear stability theory for the critical growth rate; however, we show that the results are in general agreement with the theory using our estimate for the concentration. For the range of temperature gradients and concentrations used in these experiments, the value of the critical growth rate is very sensitive to the alloy concentration, scaling approximately as c_0^{-1}, as predicted by the constitutional supercooling criterion [Eq. (1)]. This sensitivity is demonstrated in Fig. 6 by the plot of the critical growth rate predicted by linear stability theory as a function of c_0 and G for the SCN-ACE system.

In the results presented below, the labels used to distinguish particular experiments consist of three parts (SCN No., zone No., run No.), where the No. denotes an arabic number. The first identification (SCN No.) is associated with each of the 1000-mm-long samples. Within each sample, the regions over which solidification runs are performed are denoted by zone No. and the number of solidification runs performed with each zone is denoted as the run No. In this manner, the total exposure time of a particular region of the sample can be recorded precisely.

III. CALIBRATION EXPERIMENTS

A. Pure succinonitrile samples

Experiments on a sample filled with undoped SCN were performed in order to quantify the background impurity level that is necessarily introduced by any sample-preparation procedure and to verify that the concentrations of the doped samples (0.1–0.5 mol %) are significantly greater than this background level. A sample (SCN22) containing pure SCN was made using the same material transfer and sample filling steps used in the preparation of doped samples. For a temperature gradient of $G=55$ K/cm, the critical growth rate for the onset of morphology formation was measured as $V_c=8.29$ μm/s. A second run with $G=47$ K/cm over the same zone location resulted in $V_c=6.96$ μm/s.

An estimate of the impurity concentration corresponding to these observed values of V_c is calculated from the CS criterion by assuming that the impurity is acetone. Obviously, the impurity content is unknown and this assumption is made only because the thermophysical properties of the SCN-ACE system are well known. In this way the impurity concentration was estimated at less than 0.05 mol %. This result sets the bounds on the lowest levels of acetone that can be used in the experiments to give distinguishable impurity effects.

B. Calibration of acetone distribution

The usefulness of the large-scale solidification apparatus for understanding the long-time-scale dynamics of the microstructure hinges on the uniformity of the composition along the sample, so that perturbations in the composition do not introduce any systematic bias in the measurements. The theory behind these experiments is based on the very simple idea of solute segregation in a steadily solidifying, one-dimensional system without bulk convection[38] which shows that an initial uniform composition in the direction of growth will remain uniform; i.e., there is not effective segregation of the solute in the growth direction, except during transients in the growth rate (see Smith, Tiller, and Rutter[39]). The assumption of negligible bulk convection due to temperature and solute gradients is good for the very thin sample used here.

Initial experiments were performed to determine the critical growth rate at a particular temperature gradient at each end of a sample to determine the uniformity of the concentration of acetone in the sample. These results implied that the solute concentration was constant along the length of the sample. Hence we assume that the composition remains constant, if the components are thermally inert. As discussed below, this may be the poorest assumption made in the study.

C. Effect of thermal decomposition

Thermal decomposition due to exposure of the sample to the heating unit causes the total solute-impurity concentration to increase with exposure time along the length of the sample. This increase in impurity concentration may lower the critical growth rate and make the results dependent on the thermal history of the sample. This effect has been observed by previous investigators[9,24] as the hysteresis in the measurement of the critical growth rate and has been associated with the existence of a subcritical bifurcation for the planar-to-cellular transition.

The critical growth rate for the onset of cellular forms was measured as a function of the exposure time of the sample to elevated temperatures in order to investigate this hypothesis. For exposure times of less than 30 h, no hysteresis was observed, but for exposure times of 30 h or more, the effects of thermal decomposition lead to a lowering of the measured value of V_c. The translation-rate history for a representative experiment (SCN18, zone 1, run 1) of short duration is shown in Fig. 7; no hysteresis was observed, as denoted by the marks indicating the critical growth rate. Note that the sample is initially maintained for 3.0 h without translation in order to equilibrate the temperature field. The same 3.0-h equilibration time is imposed at the beginning of all experimental runs. Cellular breakup occurred at a translation rate of 1.63 μm/s for a temperature gradient of 38 °C/cm. The effective solute concentration was specified as 0.15 mol %. The sample was maintained at each translation rate for at least 60 min in order to ensure steady-state solidification rates. Subsequent increments in the solidification rate after cellular breakup lead to deeper cells with aspect ratio (depth to width) on the order of

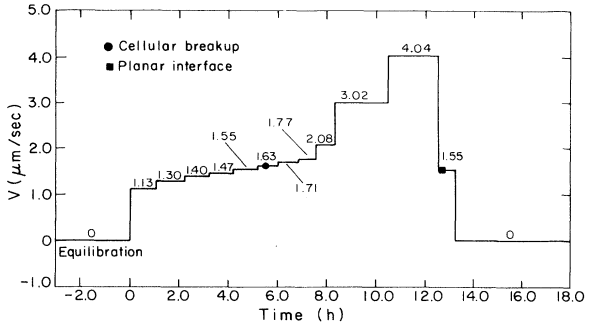

FIG. 7. Translation-rate history for (SCN18, zone 1, run 1) in which no hysteresis is observed.

10:1 at $V=4.04$ μm/s. When the solidification rate was decreased from 4.04 to 1.55 μm/s, a value slightly below the critical solidification rate (1.63 μm/s) observed at the beginning of the run, the interface became planar after only 10 min. The total exposure time of the sample to the heating unit during the experiment was 18.1 h, including the 3.0-h equilibration period prior to solidification.

Samples that were exposed to the heating unit for longer times displayed a significant decrease in V_c at the end of an experimental run relative to the value at the beginning. The translation-rate history for a representative experiment exhibiting this behavior (SCN20, zone 2, run 2) is shown as Fig. 8. The total exposure time for this run was 32.1 h. Cellular breakup occurred 30 min after a step increase in the translation rate from 0.75 to 0.83 μm/s. The cellular interface remained as the solidification rate was decreased to 0.50 μm/s, at which point the amplitudes of the cells decreased to 25 μm. Sample translation was then stopped and a planar interface evolved after 46 min. After 60 min at rest, the translation rate was increased to 0.67 μm/s and deep cells formed after 70 min. This contrasts the behavior at the beginning of the experiments where the interface remained planar at $V=0.67$ μm/s for 177 min. The results obtained from the experiments described above have been reproduced in other tests.

In a still longer experiment (SCN18, zone 1, run 3)

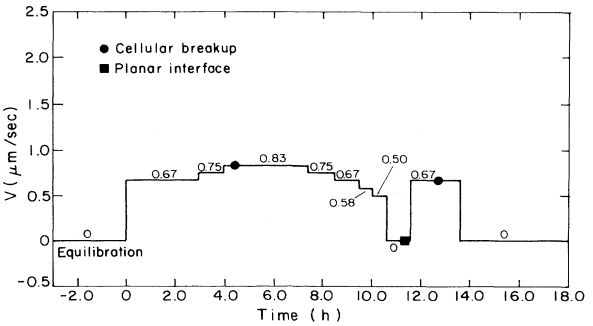

FIG. 8. Translation-rate history for (SCN20, zone 2, run 2) in which hysteresis is observed.

with a total exposure time of 49.1 h, the magnitude of the hysteresis in the critical growth rate was measured as 0.80 μm/s for $c_0 = 0.15$ mol % and $G = 21$ °C/cm. This result is very close to the hysteresis measured by Eshelman and Trivedi[9] for very similar conditions and prescribed to the existence of a subcritical bifurcation.

IV. PLANAR-TO-CELLULAR TRANSITION

Observations of the planar-to-cellular transition were performed for 21 experiments using samples based on the vacuum and nitrogen methods for sample preparation. In all of the experiments reported here, the instability of the planar interface first occurred in isolated packets of rapidly growing undulations that were separated by distances of between 600 and 1000 μm. Between these packets, the interface remained planar longer, and when undulations did begin to develop there, the local growth rate was slower than the growth rate associated with the cells in the packets.

As discussed in Lee, Tsiveriotis, and Brown,[40] the spacing between the packets were close to the λ_c predicted by linear stability theory, which suggests that they are determined by the fastest growing wavelength components at the onset of cellular solidification. The digitized interface shapes and corresponding power spectrums are presented in Figs. 9 and 10 for the experiment (SCN20, zone 3, run 2), in which of the interface spanned by the CCD camera was 6340. For this experiment, $c_0 = 0.20$ mol % and $G = 30$ °C/cm; the planar-to-cellular transition begins at 150 min after a step increase in the translation rate from 0.67 to 0.75 μm/s. The power spectrum shows peaks near 600 μm associated with the individual packets and components between 100 and 300 μm associated with the fine-scale structure. The amplitude of both components grows in time; see Figs. 9(d)–9(f) and 10(d)–10(f). At long time the cells form all along the interface; the long-time-scale microstructure is discussed in more detail below.

After 250 min at $V = 0.75$ μm/s [Fig. 10(g)], the spectral peaks at long wavelengths have disappeared and only the short-wavelength peaks remain, signaling the beginning of fully developed cellular solidification. The magnitude of the power at all wavelengths also decreased as the cellular amplitudes became smaller after initially exhibiting an overshoot to larger values. This overshoot in cell depth was observed in all experiments of the planar-to-cellular transition. Although no theory exists that describes the mechanism for this overshoot, it is probable that the phenomenon results from the undulations in the breakup packets being permitted to grow much deeper initially than can be supposed when the entire interface becomes cellular. Because solute rejection in an isolated packet is unaffected by the solute rejection of neighboring cells, lateral solute diffusion occurs more readily and allows the cell tip to extend farther into the melt than is feasible when the cells become closely packed. In this sense, small packets of cells may grow more rapidly than a front of relatively similar cells. Eventually, however, the front catches up with the packets and causes the amplitude of these cells to decrease. Our observation that the interface first breaks up into cellular packets also is evident in the pictures of Seetharaman, Eshelman, and Trivedi,[9,41,42] but has not been distinguished as a feature of the system. We return in Sec. VII to this observation.

Finer resolution in the long-wavelength portion of the power spectrum was needed to more accurately quantify the bimodal distribution shown in Fig. 10. This was ac-

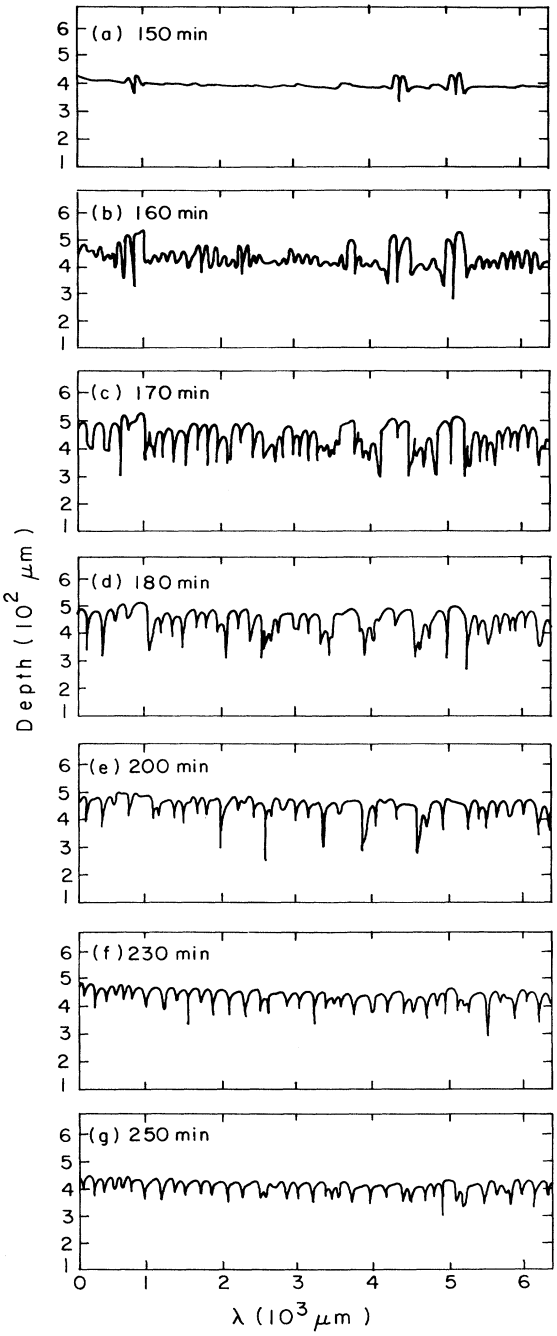

FIG. 9. Digitized interface shapes taken from (SCN20, zone 3, run 2) at (a) 150 min, (b) 160 min, (c) 170 min, (d) 180 min, (e) 200 min, (f) 230 min, and (g) 250 min after a step increase in the translation rate from 0.67 to 0.75 μm/s.

complished in the experiment (SCN20, zone 3, run 3) where the width spanned by the camera was doubled to 12 640 μm. Here $G = 24\,^{\circ}C/cm$ and cellular instability was first observed at 120 min after the step increase in V from 0.75 to 0.83 μm/s. Spectral analysis and digitized interface shapes at times between 120 and 170 min are shown as Figs. 11 and 12. Once again, the instability of

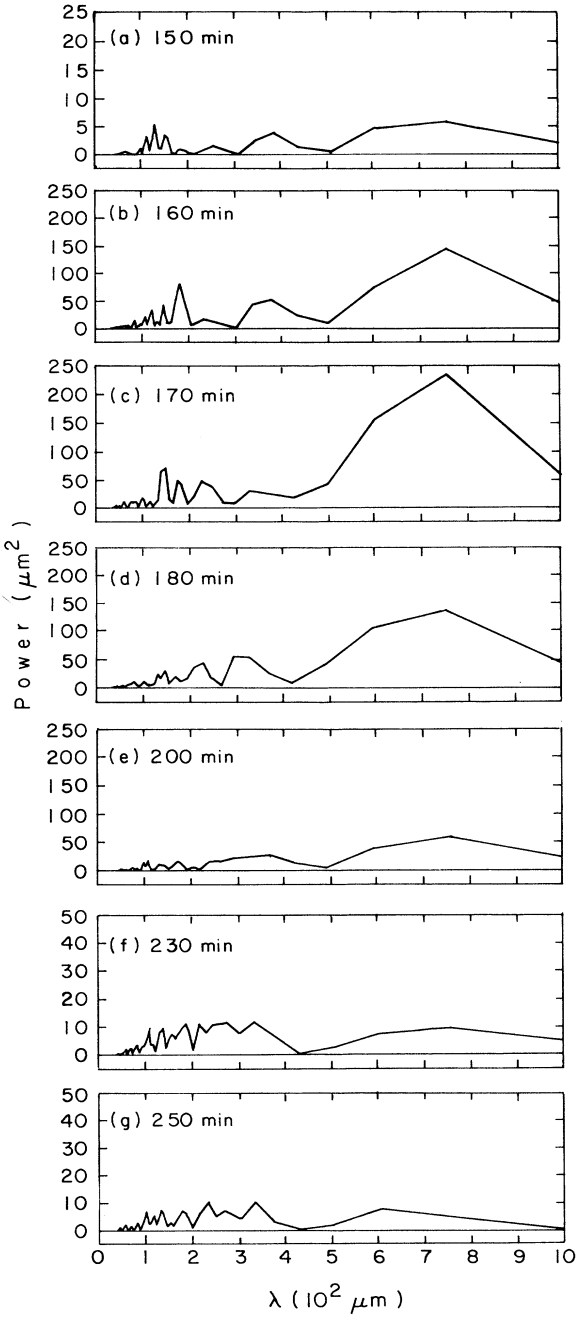

FIG. 10. Power spectra taken from (SCN20, zone 3, run 2) at (a) 150 min, (b) 160 min, (c) 170 min, (d) 180 min, (e) 200 min, (f) 230 min, and (g) 250 min after a step increase in the translation rate from 0.67 to 0.75 μm/s.

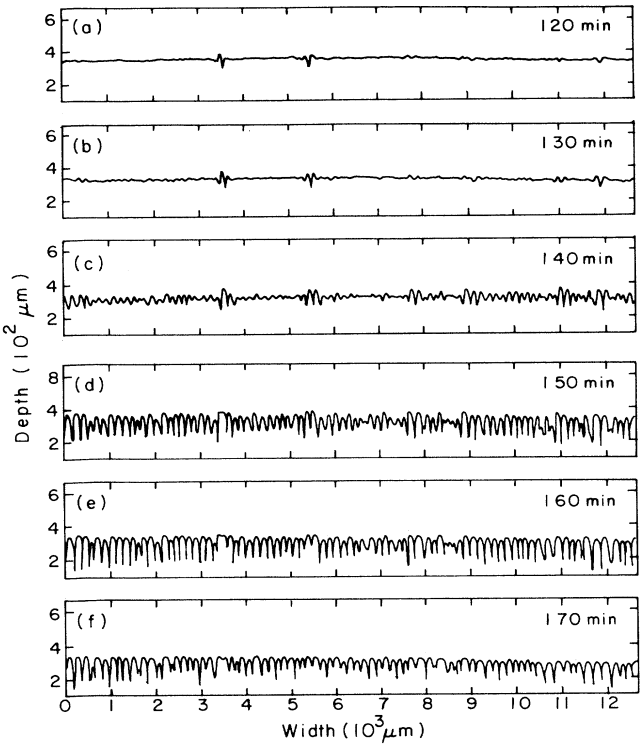

FIG. 11. Digitized interface shapes taken from (SCN20, zone 3, run 3) at (a) 120 min, (b) 130 min, (c) 140 min, (d) 150 min, (e) 160 min, and (f) 170 min after a step increase in the translation rate from 0.75 to 0.83 μm/s.

the planar interface was more pronounced at specific locations. Both the long- and short-wavelength components of the spectrum became significant at $t = 140$ min as the undulations spread over the interface. The short-wavelength components grew much faster than the long-wavelength components, in contrast to the results for (SCN20, zone 3, run 2). However, it is not clear that this observation is not an artifact of the small number of packets that exist in the measuring sample.

The interfaces shown in 10-min increments in Figs. 11(d)–11(f) also show the overshoot in amplitude. Although the importance of the long-wavelength component decayed with time, it was still present after nearly 3 h of growth as a long-wavelength modulation to a microstructure with a much smaller mean length scale. A similar spectral structure is present in Fig. 10(g).

V. CELLULAR MICROSTRUCTURES AT LONG TIMES

A. Shallow cells

The behavior of the cellular microstructures formed after long times for conditions very close to the critical growth rate was studied using samples of three different concentrations, 0.15, 0.20, and 0.35 mol %. The 0.15-mol % results were experiment (SCN18, zone 1, run 3), the 0.20-mol % results were experiments (SCN20, zone 3,

run 2) and (SCN20, zone 3, run 3), and the results for the 0.35-mol % sample were from experiment (SCN21, zone 2, run 1).

In (SCN18, zone 1, run 3), $G = 21\,^{\circ}\mathrm{C/cm}$, and the planar interface became unstable after 15 min after a step increase in V from 1.55 to 1.63 μm/s. After an additional 25 min ($t = 40$ min), fully developed cellular structures were present across the entire interface. The power spectrum and interface shape at $t = 180$ min after the step increase in V is shown in Fig. 13; there is weak selection of a critical wavelength between 160 and 200 μm. For the experiment (SCN20, zone 3, run 2), the planar interface became unstable at 150 min after a step increase in V from 0.67 to 0.75 μm/s; the interface was cellular after another 100 min of growth. The power spectrum and interface shape at $t = 330$ min are shown in Fig. 14 where the wavelength distribution spans $100 \leq \lambda \leq 500$ μm. Results for the experiment (SCN20, zone 3, run 3) are

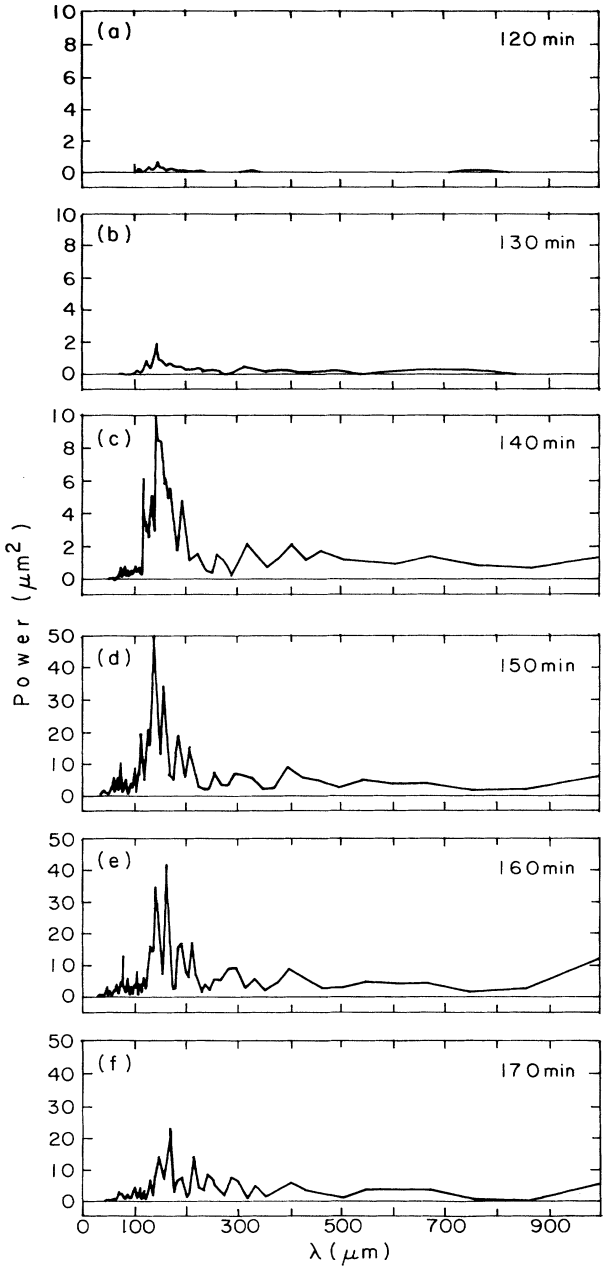

FIG. 12. Power spectra taken from (SCN20, zone 3, run 3) at (a) 120 min, (b) 130 min, (c) 140 min, (d) 150 min, (e) 160 min, and (f) 170 min after a step increase in the translation rate from 0.75 to 0.83 μm/s.

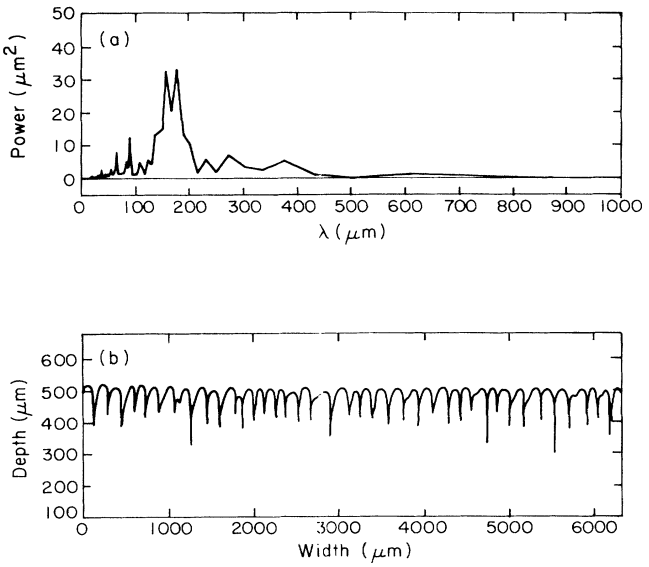

FIG. 13. (a) Power spectra and (b) digitized interface shapes taken from (SCN18, zone 1, run 3) at $t = 180$ min after a step increase in the translation rate from 1.55 to 1.63 μm/s.

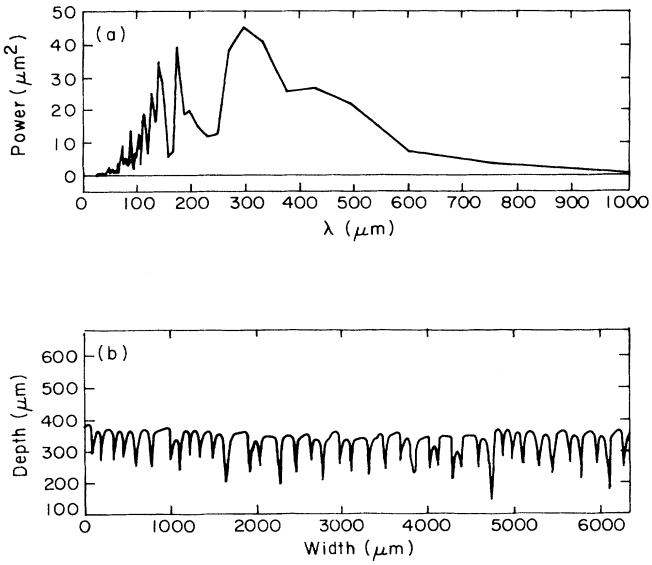

FIG. 14. (a) Power spectra and (b) digitized interface shapes taken from (SCN20, zone 3, run 2) at $t = 330$ min after a step increase in the translation rate from 0.67 to 0.75 μm/s.

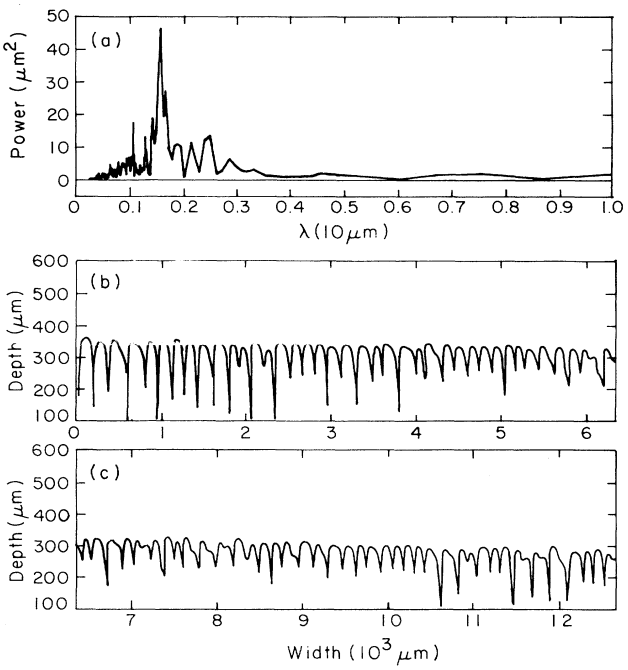

FIG. 15. (a) Power spectra and (b) and (c) digitized interface shapes taken from (SCN20, zone 3, run 3) at $t=200$ min after a step increase in the translation rate from 0.75 to 0.83 μm/s.

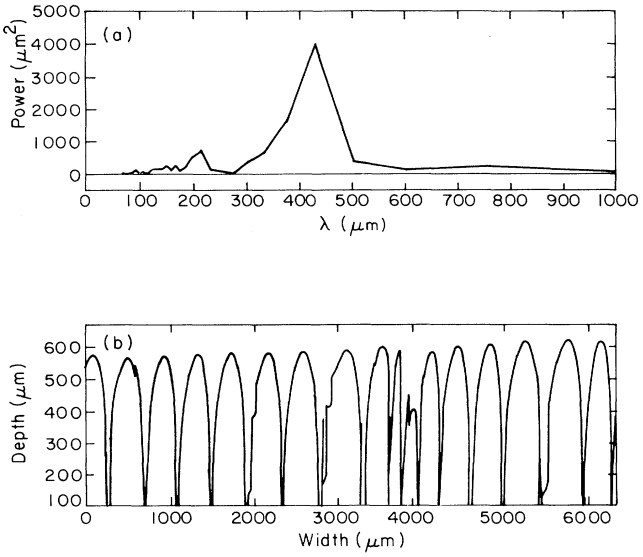

FIG. 16. (a) Power spectra and (b) digitized interface shapes taken from (SCN21, zone 2, run 1) at $t=280$ min after a step increase in the translation rate from 0.75 to 0.83 μm/s.

shown in Fig. 15 at $t=200$ min after the step increase in V from 0.75 to 0.83 μm/s. The power spectrum has a much sharper distribution about a mean wavelength of approximately 160 μm than was observed for the higher-concentration sample (SCN20, zone 3, run 2).

The wavelength distribution is dispersed for shallow cells after long solidification times, as a result of the chaotic nature of the interfacial dynamics. Tip splitting and cell elimination are observed to occur continuously for these shallow cells and lead to the *spatiotemporally chaotic* behavior that is observed. The time scale for the tip-splitting events is approximately 3500 s and agrees with those calculated numerically by Bennett and Brown.[17] These shallow cells exist for low-concentration samples at the solidification rates at which cellular breakup is first observed, and it is concluded that wavelength selection is weak for fully developed shallow cellular structures, even at long solidification it is concluded that wavelength selection is weak for fully developed shallow cellular structures, even at long solidification times. This study reports quantitative results for shallow cellular interfaces solidifying for long times due to the ability to accurately control the solidification rate near the onset of instability.

B. Deep cells

Deep solidification cells form at higher growth rates and exhibit much stronger wavelength-selection behavior after long solidification times than the shallow cells described above. This wavelength selection is shown in Fig. 16 by the interface shape and power spectrum for the experiment (SCN21, zone 2, run 1). These deep cells were observed in experiments using high-concentration samples at the solidification rates at which cellular breakup was first observed. This observation agrees with the results of others for the Br_2-CBr_4 (Ref. 5) and SCN-ACE (Ref. 41) systems. Deep cells also were observed for low-concentration samples when the solidification rate was increased beyond V_c; these results are described in Sec. VI.

VI. CELL SPACINGS WITH INCREASING SOLIDIFICATION RATES

For low-concentration samples, deep cellular shapes were produced by increasing V beyond V_c. Digitized interface shapes and power spectra are presented for the two representative experiments (SCN20, zone 3, run 2) and (SCN20, zone 3, run 3), which are shown in Figs. 17 and 18, respectively. In experiment (SCN20, zone 3, run 2), the critical growth rate was estimated as $V_c=0.75$ μm/s. The power spectrum and interface shape at $t=330$ min after the step increase in translation rate from 0.67 to 0.75 μm/s is shown in Fig. 14. As discussed above, the instability of the planar interface was detected at $t=150$ min and a fully developed cellular structure was established by $t=250$ min. The translation rate was increased at $t=330$ min to 0.83 μm/s. After 120 min at this new growth rate, the power spectrum, shown in Fig. 15(a), had a much narrower wavelength distribution centered around 200 μm with a factor of 4 increase in the power. The digitized interface shapes confirmed that the cell depths increased to values of 200–250 μm from roughly 75–150 μm for the lower growth rate; see Fig. 18(a).

Note that some of the digitized images had very steep featureless grooves. This was a result of the digitization process, in which it is assumed that the vertical coordi-

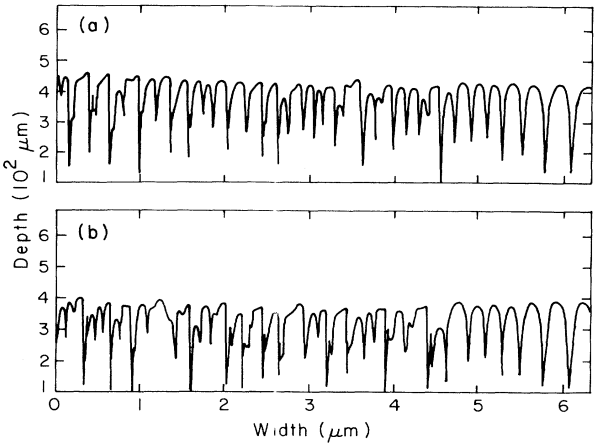

FIG. 17. Digitized interface shapes taken from (SCN20, zone 3, run 2) at (a) $t=120$ min after a step increase in the translation rate from 0.75 to 0.83 μm/s and (b) $t=60$ min after a step increase in the translation rate from 0.83 to 0.90 μm/s.

nate of the interface shape can be represented as a single-valued function of the horizontal coordinate to allow application of the FFT algorithm. These sections of almost vertical interface correspond to either reentrant cells or to shapes that are vertical within the resolution of a single pixel.

After solidification at $V=0.83$ μm/s for 120 min, the translation rate was increased to 0.90 μm/s; the evolution of the interface and power spectra are shown in Figs. 17(b) and 18(b). The power spectrum still exhibits a narrow wavelength distribution in the 100–400 μm range, but the peak was centered around the slightly higher value of 230 μm instead of 200 μm. In addition, a much stronger long-wavelength component (500–800 μm) was observed. The interface shape reveals the cause of this long-wavelength component; several regularly spaced cells have formed at width locations between 4600 and 6340 μm.

The transition between shallow chaotic cells, which exhibit broad wavelength distributions, and regularly spaced deep cells, which exhibit narrow wavelength distributions, occurs at solidification rates only slightly above V_c, and only careful control of the solidification rate allowed observation of this behavior. The (SCN20, zone 3, run 2) experiment was terminated after 60 min at 0.90 μm/s and evidence of the transition dominated by more regularly spaced deep cells was not available.

However, a higher-solidification-rate experiment was performed over the same zone (SCN20, zone 3, run 3), and the power spectrum and interface shapes for growth rates of 0.83, 1.06, and 1.13 μm/s are shown in Figs. 19 and 20. In this experiment, V_c was estimated to be 0.83 μm/s. For $V=0.83$ μm/s, the wavelength distribution was dispersed between 100 and 300 μm and the magnitude of the peak power was less than 50. The depth of the cells ranges between 100 and 200 μm. At $V=1.06$ μm/s and after 60 min of solidification, the cells were deeper (between 400 and 600 μm) and the cell spacing was more regular. At this higher solidification rate, the crystallographic orientation of the cells was offset at a slight angle to the translation direction. The cell tips actually were rounded, but have been truncated on the sides due to the digitization process. For shallow cells, truncation of the shapes of this many cells would certainly affect the wavelength distribution in the power spectrum; however, for the more regularly spaced deep cells observed at $V=1.06$ μm/s, the dominant wavelength was not affected greatly by the truncation. The power spectrum in Fig. 20(b) still exhibits dispersion about a mean wavelength, but the dominant wavelength had increased to near 300 μm.

At $V=1.13$ μm/s, the wavelength components between 250 and 300 μm clearly dominated the spectrum

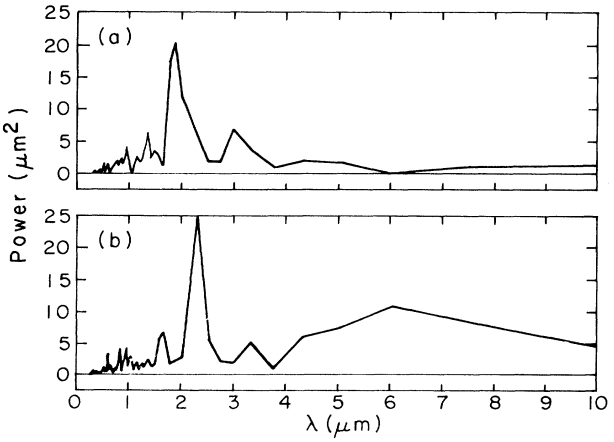

FIG. 18. Power spectra taken from (SCN20, zone 3, run 2) at (a) $t=120$ min after a step increase in the translation rate from 0.75 to 0.83 μm/s and (b) $t=60$ min after a step increase in the translation rate from 0.83 to 0.90 μm/s.

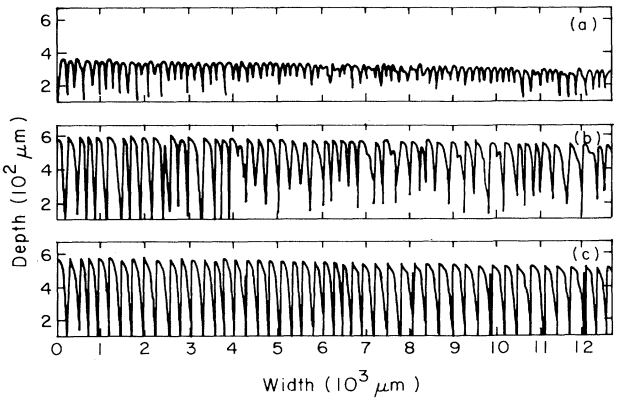

FIG. 19. Digitized interface shapes taken from (SCN20, zone 3, run 3) at (a) $t=200$ min after a step increase in the translation rate from 0.75 to 0.83 μm/s, (b) $t=60$ min after a step increase in the translation rate from 0.83 to 1.06 μm/s, and (c) $t=60$ min after a step increase in the translation rate from 1.06 to 1.13 μm/s. Note that the ordinate scale in (a) is 10 times smaller than in (b) and (c).

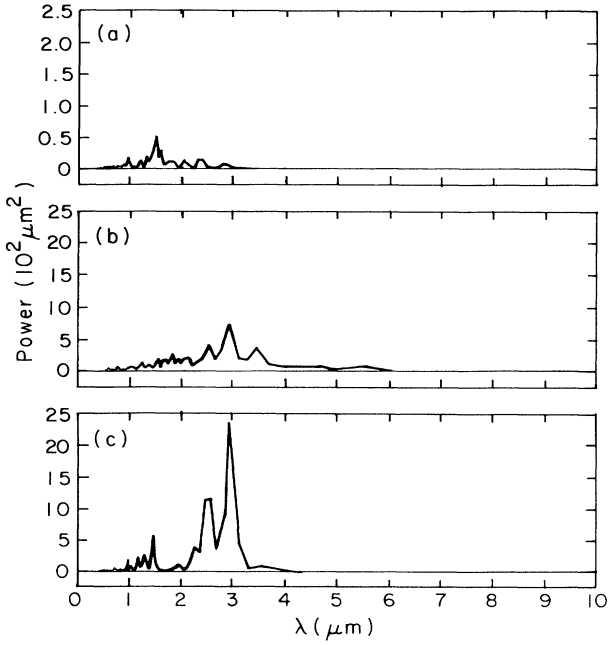

FIG. 20. Power spectra taken from (SCN20, zone 3, run 3) at (a) $t = 200$ min after a step increase in the translation rate from 0.75 to 0.83 μm/s, (b) $t = 60$ min after a step increase in the translation rate from 0.83 to 1.06 μm/s, and (c) $t = 60$ min after a step increase in the translation rate from 1.06 to 1.13 μm/s. Note that the ordinate scale in (a) is 10 times smaller than in (b) and (c).

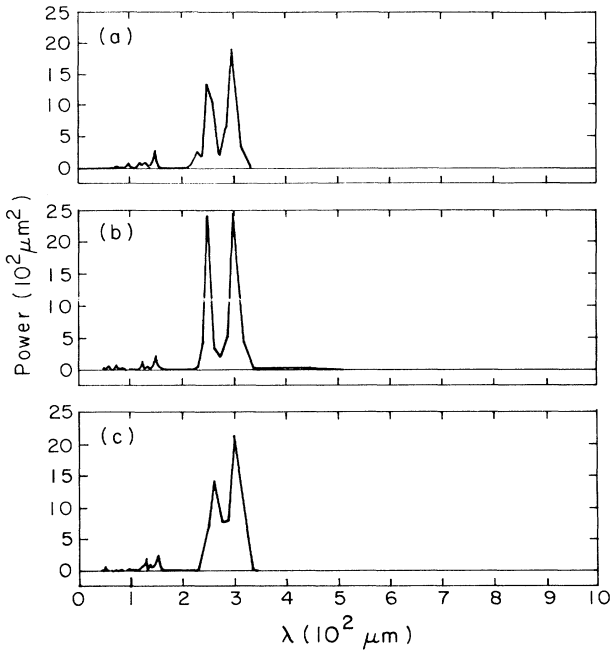

FIG. 22. Power spectra taken from (SCN20, zone 3, run 3) at (a) $t = 60$ min after a step increase in the translation rate from 1.13 to 1.22 μm/s, (b) $t = 60$ min after a step increase in the translation rate from 1.22 to 1.63 μm/s, and (c) $t = 60$ min after a step increase in the translation rate from 163 to 2.08 μm/s.

and the corresponding interface was composed of very regularly spaced deep cells. Power spectrums and interface shapes for increasing values of growth rate to 1.22, 1.63, and 2.08 μm/s are shown in Figs. 21 and 22 and were taken at 60-min intervals after step increases in the translation rate. The wavelength distribution remains narrow, and the dominant wavelengths did not change from the 250–300-μm range even though V was increased to $2.5V_c$. At solidification rates greater than 2.08 μm/s, the side undulations that are already slightly visible in Fig. 18(c) became significant and marked the transition to dendritic structures as shown in Fig. 21 taken after 60 min of growth at $V = 2.08$ μm/s. Because the cells grew at a slight angle to the translation direction, the side branches were more dominant on one side of the cells. Dendritic structures developed from very regularly spaced deep cells.

Further increases in the growth rate led to the onset of dendritic solidification with side branching initiated preferentially on a single side of the cells. An example of the

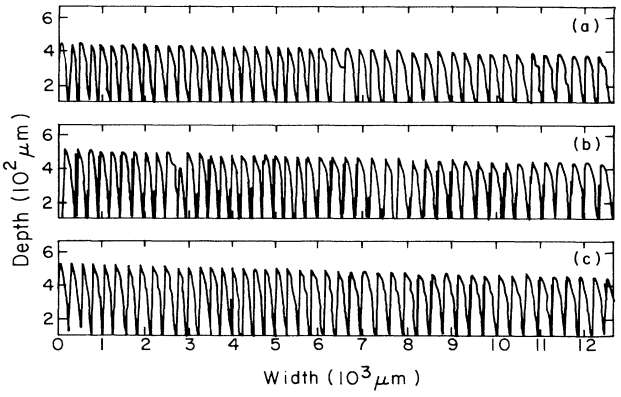

FIG. 21. Digitized interface shapes taken from (SCN20, zone 3, run 3) at (a) $t = 60$ min after a step increase in the translation rate from 1.13 to 1.22 μm/s, (b) $t = 60$ min after a step increase in the translation rate from 1.22 to 1.63 μm/s, and (c) $t = 60$ min after a step increase in the translation rate from 163 to 2.08 μm/s.

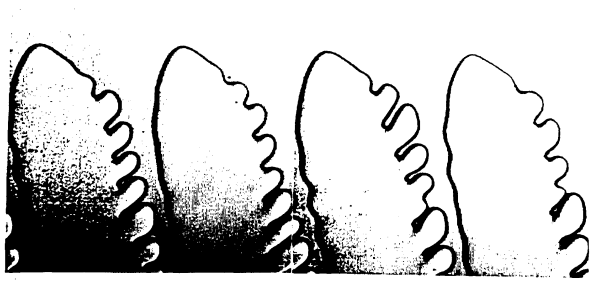

FIG. 23. Photograph of dendritic side branching developing during cellular solidification at increased growth rate; taken from (SCN20, zone 3, run 3).

phenomena is shown in Fig. 23, as taken from (SCN20, zone 3, run 2).

VII. CONCLUSIONS

The experiments reported here confirm the extreme difficulty associated with the observation of the small-amplitude cells predicted by linear stability theory. These cells only exist for an extremely narrow range of growth rates and grow very slowly from the planar state. Near onset, we observe spatiotemporally chaotic interface shapes that include a band of wavelengths with a mean value significantly below the prediction of linear stability theory. Dynamical interactions such as tip splitting, lateral migration of cells, and cell dissolution in the grooves between other cells are routinely observed on long time scales of thousands of diffusion times. These interactions are responsible for the chaotic nature of the interface. These observations are in agreement with numerical simulations for two-dimensional solidification of shallow cells,[17] which indicate a rapid decrease of the wavelength caused by nonlinear interactions caused by spatial resonance. Kassner, Misbah, and Muller-Krumbhaar[43] have shown that chaotic dynamics is possible in cellular growth because of interactions between traveling-wave states and vacillating-breathing modes characteristic of cells with dynamically changing widths.

Increasing the growth rate as little as 10% above the critical value leads to deep cells with long narrow grooves and sharpens considerably the wavelength distribution. Under these conditions a unique wavelength is selected to first order. This result does not agree with current theories of wavelength selection for deep cells,[44] which do not predict selection from a continuum of steady states within a band of values.

We observe cells to first form in packets along the solidification front spaced at intervals that most closely correspond to the wavelength λ_c predicted by linear theory. In other experiments we have measured the growth rate of the very-small-amplitude undulations from which the packets are initiated and have shown a close correspondence between this value and the growth rate $O(10^{-4}\ \mathrm{s})$ predicted by linear theory.[42] We conclude that truly sinusoidal cells at wavelength λ_c are observable for a vanishingly small range of growth rates, in agreement with simulations for the SCN-ACE alloy. The spreading of these packets across the interface leads to the irregular collections of cells seen at long times.

We believe the formation of the packets and the dynamics that follows is another nonlinear effect of the very shallow neutral stability curve. Very small perturbations to the interface, caused either by crystallographic irregularities, such as low-angle grain boundaries or local variations in the thickness of the glass sample plates, cause the interface to develop an indentation that is small, but finite, compared to the range of validity of linear theory. Solute gathers in the indentation, and it deepens rapidly because of the weakness of the restoring force of the surface energy. A deep groove forms, and small secondary cells are nucleated as ripples from its edges. These ripples spread and become the cells seen in Figs. 11(a) and 11(b). Recent numerical simulations have verified this nonlinear transient and the time scales observed in the experiments.[45]

Our experimental results also indicate that the hysteresis predicted because of the presence of initially subcritical bifurcation is not observable. Moreover, we conclude that the hysteresis observed in previous thin-film solidification experiments[5,9,24] is the result of thermal decomposition along the length of the sample, and not the result of a subcritical bifurcation in the planar-to-cellular transition. Thus the discrepancy between previous experimental observations and theory is resolved in favor of theory. Furthermore, it is concluded that for exposure times of 30 h or more, the effects of thermal decomposition begin to significantly affect the critical solidification rate obtained in our experimental system, thus limiting the number of experiments that can be performed in each zone. It is expected that for higher-concentration samples the magnitude of the thermal decomposition will be a correspondingly smaller percentage of the total solute-impurity concentration and will extend the exposure time over which experiments free of decomposition effects can be performed.

ACKNOWLEDGMENTS

This work was supported by the National Science Foundation (MSM-8710124) and by the Microgravity Sciences and Application Program of the National Aeronautics and Space Administration.

*Current address: AT&T Bell Laboratories, 600 Mountain Avenue, Room 6F-307 Murray Hill, NJ 07974.

[1]W. A. Tiller and J. W. Rutter, Can. J. Phys. **34**, 96 (1956).
[2]S. R. Coriell, G. B. McFadden, and R. F. Sekerka, Annu. Rev. Mater. Sci. **15**, 119 (1985).
[3]W. W. Mullins and R. F. Sekerka, J. Appl. Phys. **35**, 444 (1964).
[4]K. A. Jackson and J. D. Hunt, Acta Metall. **13**, 1212 (1965).
[5]S. de Cheveigné, C. Guthmann, and M. M. Lebrun, J. Phys. (Paris) **47**, 2095 (1986).
[6]A. Simon, J. Bechhoefer, and A. Libchaber, Phys. Rev. Lett. **61**, 2574 (1988).
[7]P. Kurowski, C. Guthmann, and S. de Cheveigné, Phys. Rev. A **42**, 7368 (1990).
[8]J. T. Gleeson, P. L. Finn, and P. E. Cladis, Phys. Rev. Lett. **66**, 236 (1991).
[9]M. A. Eshelman and R. Trivedi, Acta Metall. **35**, 2443 (1987).
[10]M. A. Eshelman, V. Seetharaman, and R. Trivedi, Acta Metal. **36**, 1165 (1988).
[11]P. Oswald, J. Bechhoefer, and A. Libchaber, Phys. Rev. Lett. **58**, 2318 (1987).
[12]J. Bechhoefer, P. Oswald, and A. Libchaber, Phys. Rev. A **37**, 1691 (1988).
[13]S. de Cheveigné, C. Guthmann, P. Kurowski, E. Vicente, and H. Bilone, J. Cryst. Growth **92**, 616 (1988).
[14]L. H. Ungar and R. A. Brown, Phys. Rev. B **29**, 1367 (1984).

[15]L. H. Ungar and R. A. Brown, Phys. Rev. B **31**, 5931 (1985).
[16]N. Ramprasad, M. J. Bennett, and R. A. Brown, Phys. Rev. B **38**, 583 (1988).
[17]M. J. Bennett and R. A. Brown, Phys. Rev. B **39**, 705 (1989).
[18]K. Tsiveriotis and R. A. Brown, Int. J. Numer. Methods Fluids (to be published).
[19]M. J. Bennett, K. Tsiveriotis, and R. A. Brown, Phys. Rev. B **45**, 9562 (1992).
[20]D. Haug, Phys. Rev. A **35**, 4364 (1987).
[21]P. Coullet, R. Goldstein, and G. H. Gunaratne, Phys. Rev. Lett. **61**, 2574 (1988).
[22]H. Levine and W. Rappel, Phys. Rev. A **42**, 7475 (1990).
[23]F. Heslot and A. Lichaber, Phys. Scr. T **9**, 126 (1985).
[24]S. de Cheveigné, C. Guthmann, and M.-M. Lebrun, J. Cryst. Growth **73**, 242 (1985).
[25]N. Ramprasad, Doctoral thesis, Massachusetts Institute of Technology, 1991.
[26]K. J. Frederick and J. H. Hildebrand, J. Am. Chem. Soc. **61**, 1555 (1939).
[27]L. H. Ungar and R. A. Brown, Phys. Rev. B **30**, 3993 (1984).
[28]B. Caroli, C. Caroli, and B. Roulet, J. Cryst. Growth **76**, 31 (1986).
[29]D. Kessler and H. Levine, Phys. Rev. A **39**, 3041 (1989).
[30]K. Tsiveriotis and R. A. Brown (unpublished).
[31]D. A. Kessler, J. Koplik, and H. Levine, Adv. Phys. **37**, 255 (1988).
[32]T. C. Lee, Ph.D. thesis, Department of Chemical Engineering, Massachusetts Institute of Technology, 1991.
[33]V. S. Arpaci, *Conduction Heat Transfer* (Addison-Wesley, Reading, MA, 1966).
[34]W. H. Press, B. P. Flannery, S. A. Teukolsky, and W. T. Vetterling, *Numerical Recipes* (Cambridge University Press, New York, 1986).
[35]M. A. Chopra, M. E. Glicksman, and N. B. Singh, J. Cryst. Growth **92**, 543 (1988).
[36]M. A. Chopra, M. E. Glicksman, and N. B. Singh, Metall. Trans. A **19**, 3087 (1988).
[37]M. E. Glicksman, R. J. Schaefer, and J. D. Ayers, Metall. Trans. A **7**, 1747 (1976).
[38]W. A. Tiller, K. A. Jackson, J. W. Rutter, and B. Chalmers, Acta Metall. **1**, 428 (1953).
[39]V. G. Smith, W. A. Tiller, and J. W. Rutter, Can. J. Phys. **33**, 723 (1955).
[40]J. T. C. Lee, K. Tsiveriotis, and R. A. Brown, J. Cryst. Growth **121**, 536 (1992).
[41]M. A. Eshelman and R. Trivedi, Scr. Metall. **22**, 893 (1988).
[42]V. Seetharaman, M. A. Eshelman, and R. Trivedi, Acta Metall. **36**, 1175 (1988).
[43]K. Kassner, C. Misbah, and H. Muller-Krumbhaar, Phys. Rev. Lett. **67**, 1551 (1991).
[44]T. Dombre and V. Hakim, Phys. Rev. A **36**, 2811 (1987).
[45]K. Tsiveriotis, J. T. C. Lee, and R. A. Brown (unpublished).